Laser direct writing and characterizations of flexible piezoresistive sensors with microstructures

Chenying Zhang[1], Wei Zhou[1]*, Da Geng[1], Cheng Bai[1], Weida Li[1,2], Songyue Chen[1]*, Tao Luo[1], Lifeng Qin[1] and Yu Xie[1]

[1]Department of Mechanical & Electrical Engineering, Xiamen University, Xiamen 361101, China; [2]College of Information Science and Engineering, Northeastern University, Shenyang 110004, China.

*Correspondence: W Zhou, E-mail: weizhou@xmu.edu.cn; SY Chen, E-mail: s.chen@xmu.edu.cn

This file includes:

Supplementary information for this paper is available at https://doi.org/10.29026/oea.2021.200061

Section 1: Morphologies of materials

Figure S1 shows the morphologies of MWCNTs, PDMS and MPC. As shown in Fig. S1(a), MWCNTs show a high length-diameter ratio and get tangled up with each other. It is attributed to the Van der Waals force between MWCNTs. Consequently, MPC show much rougher surface than pure PDMS due to the internal agglomeration of MWCNTs, as shown in Fig. S1(b) and Fig. S1(c).
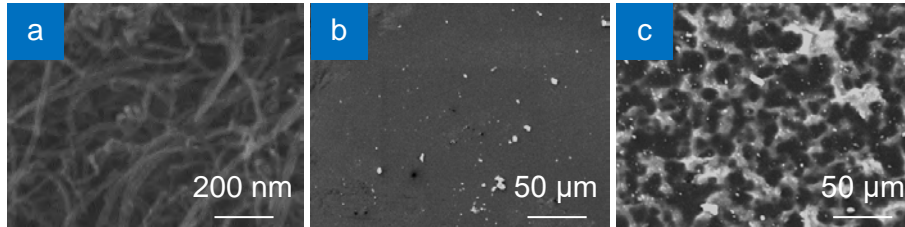

Fig. S1 | SEM images of (a) MWCNTs, (b) PDMS, (c) MPC.

Section 2: Evaluation of mechanical properties

The mechanical evaluation system is shown in Fig. S2.

Fig. S2 | Stretching test of materials.

The strain along stretching direction (ε_z) is calculated as Eq. S1:

$$\varepsilon_z = \frac{\Delta L}{L_0} \times 100\%, \tag{S1}$$

where ΔL and L_0 refer to the length variation and original length of the testing sample, respectively.

On the cross section of the testing sample, the width w and thickness t direction (ε_x) are calculated as Eq. S2:

$$\frac{w}{w_0} = \frac{t}{t_0}, \tag{S2}$$

where w_0 and t_0 refer to the original width and original thickness of the testing sample, respectively.

The tensile stress (σ_z) is calculated as Eq. S3:

$$\sigma_z = \frac{F_z}{wt}, \tag{S3}$$

where F_z refers to tensile force.

The relationships of ε_z and σ_z can be described by Young's modulus (E), as shown in Eq. S4:

$$\sigma_z = E\varepsilon_z \,, \tag{S4}$$

Consequently, E of testing samples can be evaluated by slopes of σ_z-ε_z curves.

Section 3: Variation of laser power and pulse with frequency

Figure S3 shows the variation of laser power and pulse with repetition frequency at $Q = 1$. Laser pulse is increased with the increase of repetition frequency. When repetition frequency is below 80 kHz, laser power increases with the increasing repetition frequency. When repetition frequency exceeds 90 kHz, laser power decreases with the increasing repetition frequency.
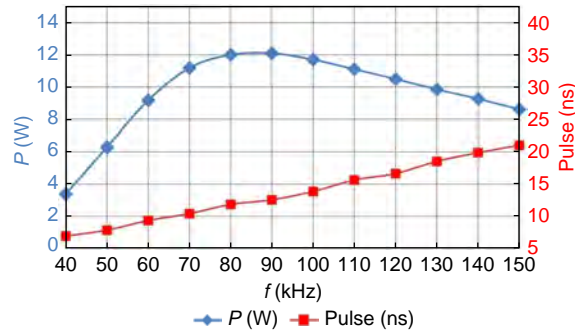

Fig. S3 | Variation of laser power and pulse with repetition frequency at $Q = 1$.

Section 4: SEM images of microstructures fabricated with different laser parameters

Figure S4 shows surface morphologies of the microstructures fabricated with different laser parameters. When laser repetition frequency varied from 35 kHz to 45 kHz, laser power varied in an approximate range of 2~5 W, which brought about significant impacts in morphology of microstructures. When laser scanning speed varied from 100 mm·s⁻¹ to 200 mm·s⁻¹, obvious difference in morphology of the microstructures could be found, which can be attributed to the significant variation in the laser energy density. When laser repetition frequency was below 40 kHz, laser path can be found on the substrates and the microstructures had relative small size. When laser repetition frequency was set to 45 kHz, the laser path disappeared from substrates because a higher energy density induced significant ablation and quantities of particles can be found around the microstructures, which indicated destruction to the microstructures.
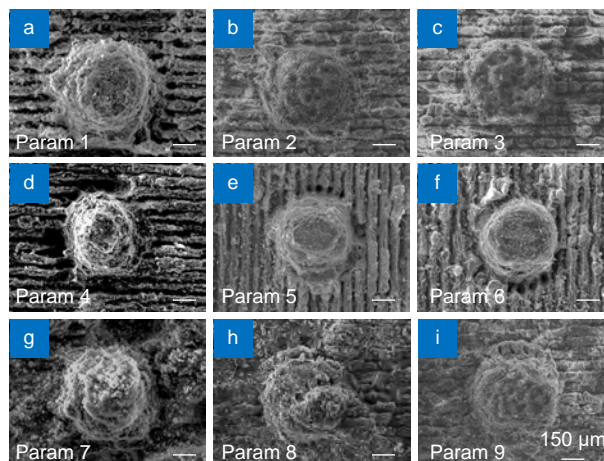

Fig. S4 | Surface morphologies of microstructures fabricated with different laser parameters imaged by a SEM. Abbreviations | Param 1: f = 35 kHz, v = 100 mm·s⁻¹; **Param 2**: f = 35 kHz, v = 150 mm·s⁻¹; **Param 3**: f = 35 kHz, v = 200 mm·s⁻¹; **Param 4**: f = 40 kHz, v = 100 mm·s⁻¹; **Param 5**: f = 40 kHz, v = 150 mm·s⁻¹; **Param 6**: f = 40 kHz, v = 200 mm·s⁻¹; **Param 7**: f = 45 kHz, v = 100 mm·s⁻¹; **Param 8**: f = 45 kHz, v = 150 mm·s⁻¹; **Param 9**: f = 45 kHz, v = 200 mm·s⁻¹.

Section 5: Sensitivities of flexible piezoresistive sensors fabricated by different laser parameters

Figure S5 shows sensitivity of flexible piezoresistive sensors fabricated by different laser parameters. Laser parameters significantly affected the sensitivity and the performance of flexible piezoresistive sensors through modulating the surface morphologies of microstructures.
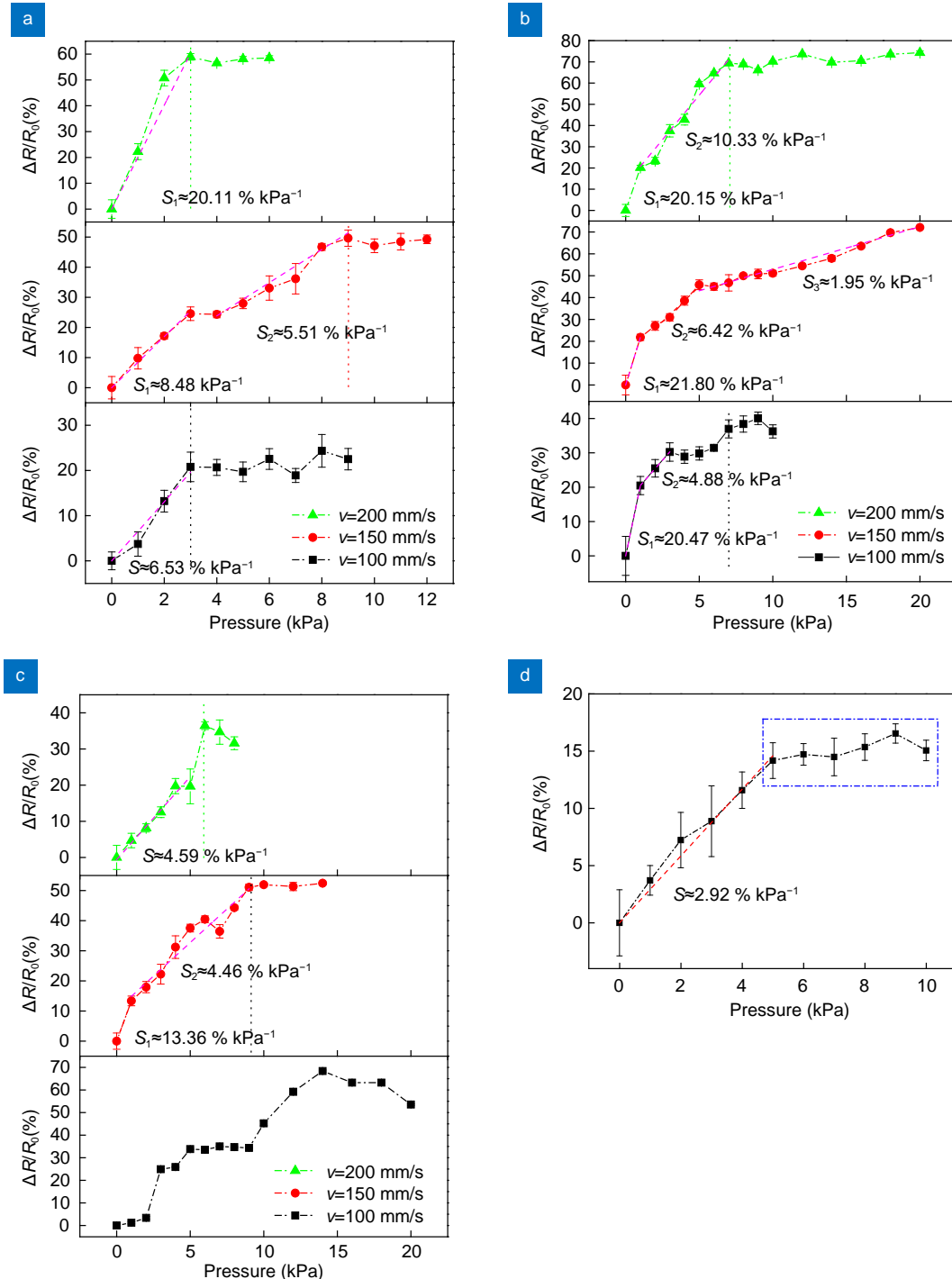
Fig. S5 | Sensitivities of flexible piezoresistive sensors fabricated by different laser parameters (**a**) *f*=35 kHz. (**b**) *f*=40 kHz. (**c**) *f*=45 kHz. (**d**) without microstructures.

Section 6: Supplementary videos

Video S1. Resistance variation of the flexible piezoresistive sensor for dynamic pressure about 2 kPa.

Video S2. Application of the piezoresistive sensor in LED brightness controlling by finger pressing.

Video S3. Resistance variation of the flexible piezoresistive sensor in wrist pulse detection.

Video S4. Resistance variation of the flexible piezoresistive sensor in voice recognition.

Section 7: Supplementary tables

Table S1 | Parameters of the SEAL-355-10 laser.

Parameter	Symbol	Value	Unit
Laser wavelength	λ	355	nm
Repetition frequency	f	≤300	kHz
Average output power	P	≤12	W
Pulse width	τ	≤12	ns
Beam quality factor	M^2	≤1.2	

Table S2 | Parameter ranges for laser processing of the flexible piezoresistive sensor with microstructures.

Parameters	Symbols	Units	Experimental values
Laser repetition frequency	f	kHz	35, 40, 45
Scanning speed	v	mm s^{-1}	100, 150, 200
Scanning times	n		4
Q pulse width	Q	μs	1

Table S3 | Comprehensive comparisons between this work and references[1–8].

Ref.	Microstructures	Methods	Maximum sensibility[% kPa^{-1}]	Detection limits[kPa]	Response time[ms]
1	Multilayer	Chemical synthesis	20	40	30
2	Fabric network	Dipping, thiolation	8.36	200	87
3	Hierarchical microstructures	Molding, etching, thermal oxidation, CVD	13.7	12	40
4	Porous material	Printing	0.04	40	Not given
5	Fish scale like	Curing on water surface, dipping	70.86	5	Not given
6	Hierarchical porosity	3D Printing	6.7	800	20
7	Irregular microstructures	Molding, thermal reduction	25.1	40	80
8	Hierarchical wrinkles	Thermal deforming, stretching, thermal reduction	0.98	4	100
This work	Curved cone-like microstructures	Laser direct writing	21.80	20	100

References

1.   Ma YN, Liu NS, Li LY, Hu XK, Zou ZG et al. A highly flexible and sensitive piezoresistive sensor based on MXene with greatly changed inter-layer distances. *Nat Commun* **8**, 1207 (2017).

2.   Zhang L, Li HQ, Lai XJ, Gao TY, Yang J et al. Thiolated Graphene@Polyester Fabric-Based Multilayer Piezoresistive Pressure Sensors for Detecting Human Motion. *ACS Appl Mater Interfaces* **10**, 41784–41792 (2018).

3.   Bae GY, Pak SW, Kim D, Lee G, Kim D et al. Linearly and Highly Pressure-Sensitive Electronic Skin Based on a Bioinspired Hierarchical Structural Array. *Adv Mater* **28**, 5300 (2016).

4.   Liu L, Huang Y, Li FY, Ma Y, Li WB et al. Spider-web inspired multi-resolution graphene tactile sensor. *Chem Commun* **54**, 4810–4813 (2018).

5.   Wang J, Tenjimbayashi M, Tokura Y, Park JY, Kawase K et al. Bionic Fish-Scale Surface Structures Fabricated via Air/Water Interface for Flexible and Ultrasensitive Pressure Sensors. *ACS Appl Mater Interfaces* **10**, 30689–30697 (2018).

6.   Wang Z, Guan X, Huang H, Wang H, Lin W et al. Full 3D Printing of Stretchable Piezoresistive Sensor with Hierarchical Porosity and Mul-timodulus Architecture. *Adv Funct Mater* **29**, 1807569 (2019).

7.   Pang Y, Zhang KN, Yang Z, Jiang S, Ju ZY et al. Epidermis Microstructure Inspired Graphene Pressure Sensor with Random Distributed Spinosum for High Sensitivity and Large Linearity. *ACS Nano* **12**, 2346–2354 (2018).

8.   Chang TH, Tian Y, Li CS, Gu XY, Li KR et al. Stretchable Graphene Pressure Sensors with Shar-Pei-like Hierarchical Wrinkles for Collision-Aware Surgical Robotics. *ACS Appl Mater Interfaces* **11**, 10226–10236 (2019).